

COMPUTATIONAL INVESTIGATION OF ICING CONTAMINATION ON AIRFOIL

Thaís Bortholin, Fernando M. Catalano
University of São Paulo, Brazil
thais.bortholin@gmail.com; catalano@sc.usp.br

Keywords: *airfoil, ice accretion, CFD*

Abstract

Icing accretions can modify the geometry of an airfoil significantly and they affect its performance. Two categories of icing accretions were analyzed in NACA 0012 airfoil through the effects in the force as well as in pressure distribution via numerical simulations. The results were compared with others computational experiments and measurements in wind tunnel of references in order to validate this research.

1 Introduction

Icing accretions hazards have been studied in order not only to understand in which situation they appear and make possible to predict their formation but also to evaluate the performance depreciation they cause. This information is quite important because it is linked to certification: FAR 25 [1], for example, has a specific envelope just for icing certification based on previous studies, such as Hacker [2]. The present study analyses Glaze icing which was tested in a wind tunnel by Bragg [3] and simulated using computational methods by Bragg and Loth [4]. Another analysis, a Rime icing study, was performed using Cao [5] reference. A hybrid C shaped mesh prepared in ICEM [6] was used since it adapts better to unusual airfoil geometry. However, a grid analysis was also performed.

3 Nomenclature

AOA	Angle of attack
C_d	2D drag coefficient
C_p	Pressure coefficient
C_l	2D lift coefficient

4 Clean airfoil analyses

Several turbulence models were tested with two different meshes approaches in order to verify their influence in the simulations so that a tradeoff analysis could be performed. The models tested were chosen based on crescent complexity.

Spalart-Allmaras is a one-equation model. It does not calculate the turbulence kinetic viscosity. Different from other versions of this model algorithm, the one used in Fluent [7] is able to identify whether the mesh is not fine enough and, if so, use a wall function treatment. However, grid resolution in buffer layer with $3 < y^+ < 30$ should be avoided since it corresponds to the edge of the wall function usage threshold.

The 2-equation Realizable $k \epsilon$ model is based in transport equations for the turbulence kinetic energy (k) and its dissipation rate (ϵ). The Realizable term refers to the satisfaction of

some mathematical variables of Reynolds stresses and Realizable $k \varepsilon$ has a different approach for ε equation, based on vorticity fluctuation.

The 2-equation $k \omega$ model is based on transport equations for the turbulence kinetic energy (k) and its specific dissipation rate (ω). *SST* $k \omega$ model differs from the standard, mainly, because it considers the effects of turbulent shear stress transport.

At last, 4-equation *Shear Stress Transport* model, which is the *SST* $k \omega$ transport equations summed up to two more equations was employed. The additional equations involves new terms as intermittency (measure of the probability that a given point is located inside a turbulent region) and transition onset criteria.

An important detail is that $k \omega$ and $k \varepsilon$ can employ an enhanced wall treatment: if the near wall mesh is fine enough to resolve the viscous sublayer, which means $y^+ \approx 1$, the equations are solved in the usual way. On the other hand, if the mesh is coarse near the wall, a wall function treatment is imposed. It can be done calculating the wall-normal distance at the cell centers, as it is shown in Equation 1.

$$y = \min\|\vec{r} - \vec{r}_w\| \quad (1)$$

To evaluate the strength and weakness of the models is crucial to allow a careful tradeoff study and to enable a reliable result. An expensive model, with additional equations, confers more accuracy to the stall prediction. However, this model consumes more CPU time to be solved and it requires more input parameters to be set, whose determination is not simple. Because of that, a complexity model should be chosen only when the analysis intended makes it necessary.

During the mesh study an important parameter to be evaluated is y^+ - the dimensionless distance from the wall - a variable based on the distance from the wall to the first node and the wall shear stress, as it is possible to be noticed in Equation 2, where Δy is the distance from the wall and u_τ is the friction velocity.

$$y^+ = \frac{\rho \Delta y u_\tau}{\mu} \quad (2)$$

At the present analyses, two mesh strategies were evaluated: hybrid mesh with patch dependent algorithm and prism layers, a 2d approximation, and a hexa structured approach. Although y^+ is a parameter that does not only depend on mesh geometric definitions but also dependent on the flow near the wall, represented by u_τ term, a progression of Δy distance was used to build up 3 meshes of each strategy so that a y^+ progression could be obtained. In order to avoid excessive variables and keep the consistence of the study, the number of “prism” layers and growth ratio were kept constant in the hybrid meshes. These analyses were performed with the 4 turbulence models already mentioned.

Fig. 1 and Fig. 2 show the meshes employed in the study. The first element height was varied from 10^{-4} mm to 10^{-6} mm, from the first to the third mesh in both approaches (based on a unitary chord). Since the growth ratio and the number of “prism” layer were kept the same, it is possible to notice that the total height of the prism layer is not the same. The total height influence in the result was not evaluated in order to minimize the number of mesh input parameters.

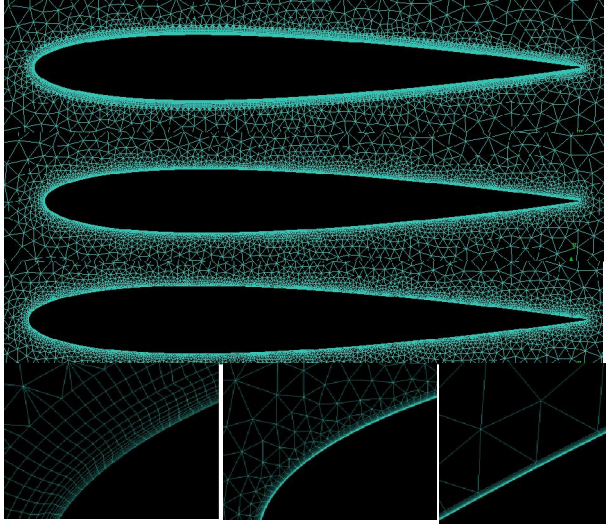


Fig. 1 – Hybrid meshes used in the study

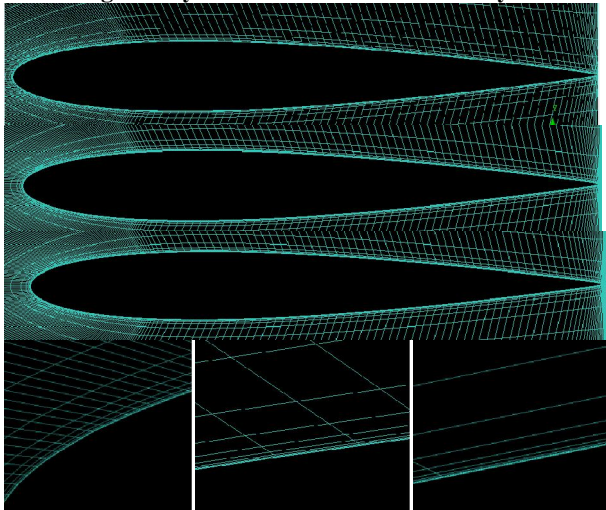


Fig. 2 – Hexa meshes used in the study

The *Courant* number employed was a ramp of 5 to 50 during the first 200 iterations. An adaption resource of Fluent [7] was toggled on: if it is necessary, the solver performs an automatic *CFL* reduction and recalculates the iteration. Time step is proportional to *CFL* value.

Harris [7] NACA 0012 wind tunnel data were employed to validate the found results. Harris [7] experiment was performed at $Re = 3 \text{ million}$ and $Mach = 0.30$. The ideal air gas assumption was adopted. The wind tunnel conditions were reproduced using Equation 3 and Equation 4 shown bellow.

$$Re = \frac{\rho U d}{\mu} = \frac{\rho d}{\mu} \cdot M \cdot c \quad (3)$$

$$= \frac{\rho d}{\mu} \cdot M \cdot M \sqrt{\gamma R T} \quad (4)$$

$$P = \rho R T$$

RMS (root mean square) error of C_d could not be determined because the experimental reference data were extracted via digitalization and, therefore, they do not present the same discretization of angle of attack on the runs performed and a polynomial trend line was not able to fit the reference curve. Because of that, it was used, in the present analyses, the absolute error for both C_d and C_l values, using two references relevant to the study (minimum and maximum values, respectively). It was done a total of 24 numeric simulations, using all the meshes presented above and the quoted turbulence models.

From Table 1 to Table 4 it is presented the error values for hexa meshes. It can be noticed that as y^+ becomes lower (it means a finer mesh), C_l^{max} error is minimized. Nevertheless, this behavior was not seen in Spalart-Allmaras and Shear Stress Transport model, both presenting the opposite trend. Considering C_d^{min} , the error responses were the same: the error was minimized with lower y^+ just for $k \epsilon$ and $k \omega$ models. This behavior could be justified since Spalart-Allmaras model was used in a range of values not recommended, which is inside the gap of the solver algorithm as it was mentioned previously. In *SST* model, the numerical solution for transition locations requires the input variables to be set precisely, which cannot be done just using software default parameters.

Table 1 - Results for hexa mesh with Spalart-Allmaras model

Mesh	Coarse	Medium	Fine
Error C_l^{max}	14.15%	2.53%	8.08%
Error C_d^{min}	0.38%	0.64%	0.73%
AOA stall [°]	14	13	13
y^+	5.75	0.63	0.07

Table 2 - Results for hexa mesh with Realizable $k \epsilon$ model

Mesh	Coarse	Medium	Fine
Error C_l^{max}	7.99%	6.54%	5.61%
Error C_d^{min}	0.35%	0.22%	0.14%
AOA stall [°]	14	14	14
y^+	5.32	0.50	0.04

Table 3 - Results for hexa mesh with $k \omega$ model

Mesh	Coarse	Medium	Fine
Error C_l^{max}	8.75%	6.54%	0.15%
Error C_d^{min}	0.79%	0.18%	0.02%
AOA stall [°]	14	14	13
y^+	6.26	0.46	0.04

Table 4 - Results for hexa mesh with Shear Stress Transport model

Mesh	Coarse	Medium	Fine
Error C_l^{max}	5.27%	0.16%	5.25%
Error C_d^{min}	0.30%	0.34%	0.39%
AOA stall [°]	13	14	13
y^+	5.88	0.54	0.04

In the hybrid mesh analyses it has not been found any well-defined trend. The y^+ values obtained in the hybrid meshes were quite close to the ones obtained in the hexa meshes, what indicates that the first element height is a dominant factor in y^+ . It was also concluded that higher accuracy in the solution is not linked just to lower values of y^+ .

From Table 5 to Table 8, it can be perceived that C_l^{max} error decreases whereas refinement increases, except in *SST* model. This was a similar behavior to the hexa meshes. On the other hand, C_d^{min} error has not decreased with lower y^+ . This apparent inconsistency is related to the input constraints: as it was fixed the number of layers and the quad growth ratio, the mesh generator calculated the total height of

the “prism” layer. For this reason, it is difficult to see the difference among the meshes in Fig. 2. With the parameters fixed as described above, when the y^+ value is decreased, a restriction of quads occurs near the profile wall. This invalidates the accurate flow reproduction immediately after the profile. The representation of this region is also essential to capture the flow around the airfoil in a realist manner, since there are inside this region some phenomena, as eddies development, which influence the behavior of flow near the wall area.

Therefore, there should be a hybrid mesh equivalent to an hexa one, with quad elements just in the region necessary to represent accurately the flow around the wall. Considering the input parameters to build up a hybrid mesh, the number of layers should be also evaluated, but not only the first element height fine enough to assure a lower y^+ . The subsequent studies have been performed with a hybrid mesh using additional quads layers in order to preserve the flow aspects not just near the wall.

Table 5 - Results for hybrid mesh with Spalart-Allmaras model

Mesh	Coarse	Medium	Fine
Error C_l^{max}	13.37%	24.78%	24.79%
Error C_d^{min}	1.39%	0.79%	0.86%
AOA stall [°]	14	13	13
y^+	7.56	0.91	0.09

Table 6 - Results for hybrid mesh with Realizable $k \epsilon$ model

Mesh	Coarse	Medium	Fine
Error C_l^{max}	17.65%	15.11%	12.69%
Error C_d^{min}	0.35%	0.38%	2.22%
AOA stall [°]	14	14	14
y^+	7.66	0.74	0.07

Table 7 - Results for hybrid mesh with $k \omega$ model

Mesh	Coarse	Medium	Fine
Error C_l^{max}	12.05%	7.73%	7.23%
Error C_d^{min}	2.07%	0.24%	0.28%
AOA stall [°]	14	14	15

y^+	7.53	0.73	0.06
-------	------	------	------

Table 8 - Results for hybrid mesh with *Shear Stress Transport* model

Mesh	Coarse	Medium	Fine
Error C_l^{max}	8.69%	7.31%	14.17%
Error C_d^{min}	0.11%	0.22%	0.31%
AOA stall [°]	14	13	12
y^+	7.20	0.73	0.07

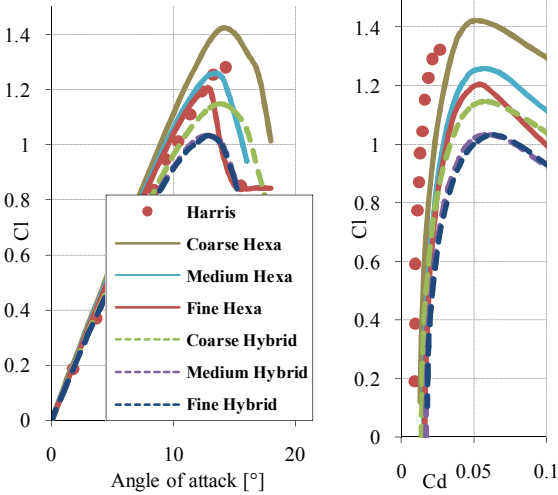


Fig. 3 - C_l versus angle of attack for Spalart-Allmaras

Fig. 4 - Drag Polar for Spalart-Allmaras

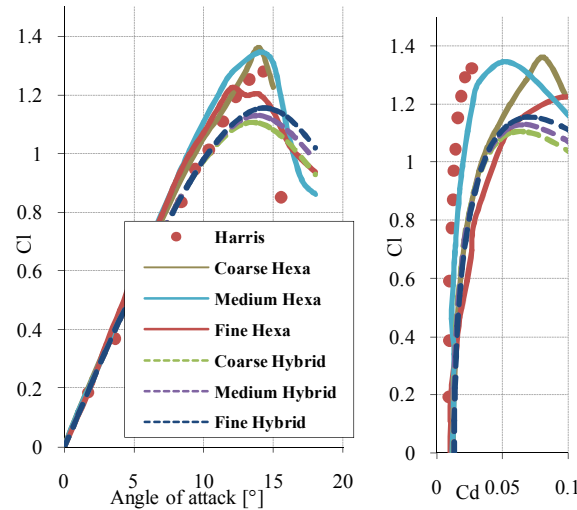


Fig. 5 - C_l versus angle of attack for Realizable $k \epsilon$

Fig. 6 - Drag Polar for Realizable $k \epsilon$

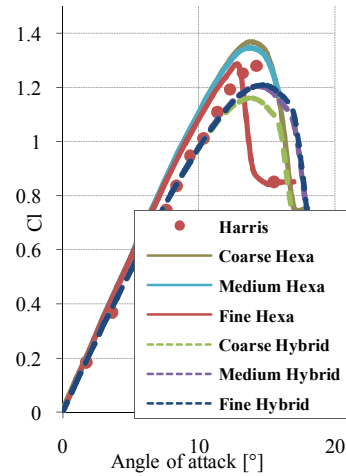


Fig. 7 - C_l versus angle of attack for $k \omega$

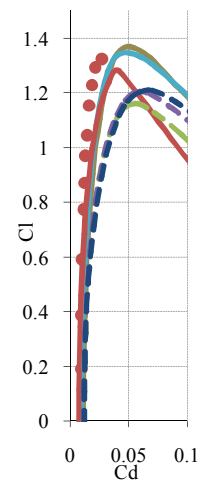


Fig. 8 - Drag Polar for $k \omega$

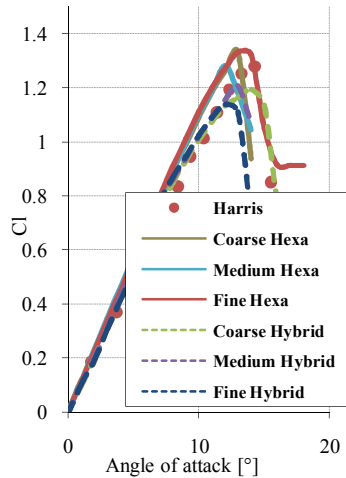


Fig. 9 - C_l versus angle of attack for SST

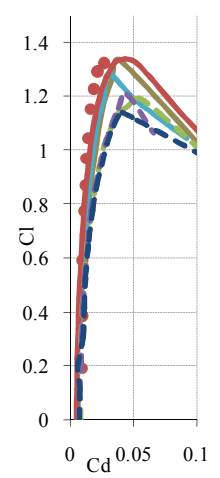


Fig. 10 - Drag Polar for SST

5 Rime Icing Analysis

The ice accretion geometry analyzed was taken from Cao [5]; it is a leading edge ice accretion with an angle of attack of 4° (ice distribution is dependent on the angle of attack at the moment of the ice formation). LWC (liquid water content) was 1.0 g/m^3 . This value represents the water mass in liquid state inside a cloud per unit of its volume and it allows the distinction between ice crystals and liquid droplets). Another important parameter in ice accretion is the MVD (median volumetric diameter) and it represents the diameter of the

droplets inside the cloud. The MVD of the studied accretion was of 20 μ m.

LWC and MVD are employed as parameters by FAR 25 [1] in order to define which is the acceptable limit of ice accretion. The flight envelope is determined considering, in addition to these variables, room temperature and the interaction among them. The maximum limit for icing is classified as intermittent and continuous.

These flight envelopes are shown in Fig. 11 and Fig. 12. It is possible to notice the low maximum vertical range, 6500 ft (1981.2 m), lower than the service ceiling of an aircraft. This is justified by Hacker [2], who mentions that 89% of ice accretions come from stratiform clouds (continuous form) and happen in less than 5000 ft of vertical range. Since the temperature was not given by the reference, it is not possible to find the geometry properly in the envelope.

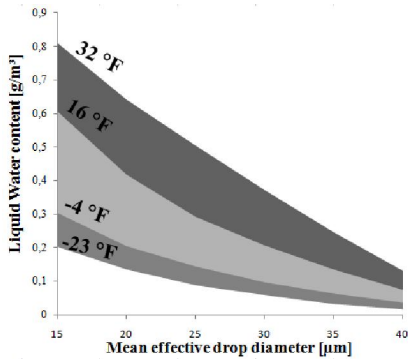


Fig. 11- Envelope for Continuous Maximum (Stratiform Clouds)

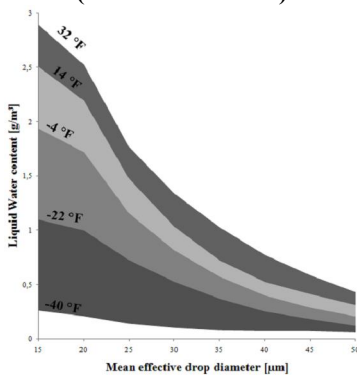


Fig. 12 - Envelope for Intermittent Maximum (Cumuliform Clouds)

Fig. 13 shows the mesh used in the analysis which was chosen based on the previous results.

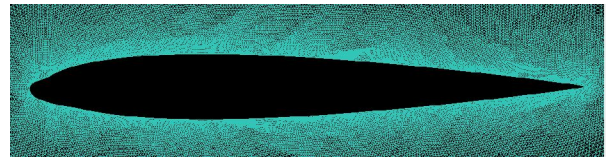


Fig. 13 - Mesh around rime ice airfoil

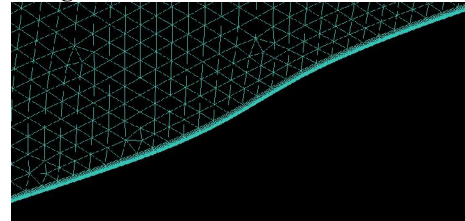


Fig. 14 - Close up view of the mesh around rime ice airfoil

The angle of attack used is 4° with $Re = 1.5$ million and $Mach = 0.20$. The turbulence model employed was 4-equation Shear Stress Transport.

In Fig. 15 it is shown the comparison of pressure coefficient between simulated airfoil and the one obtained from Cao [5]. Despite some differences, especially at the suction peak, the distributions presented a good coherence.

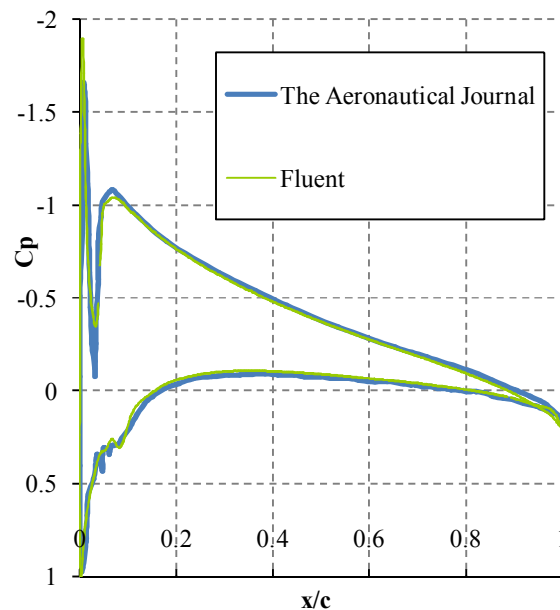


Fig. 15 - Pressure distribution comparison for 4.17° of angle of attack

Fig. 16 shows pressure coefficient

comparison between the clean airfoil and that one with rime ice for zero angle of attack. At first sight, it can be verified the loss of symmetric characteristics, what can be apprehended through the curve: the suction peak is no longer well defined as in the clean airfoil, decreasing about 3%, and the upper and lower surface are not coincident anymore.

As the angle of attack increases, the trend is the same: the suction peak goes forward to the leading edge and the flow suffers a pressure recuperation after the intersection region between the degraded region and the clean airfoil; this pressure variation is kept constant, about 35%, despite the increasing of the angle of attack as could be noticed observing the pressure distributions for other angles of attack.

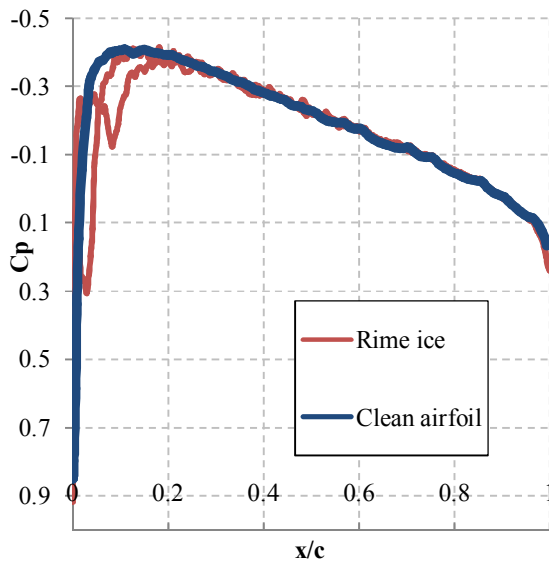


Fig. 16 - Pressure distribution comparison for 0° of angle of attack

In Fig. 18 it is seen the pressure difference between the clean airfoil and the degraded, for the same conditions. In the colormap, the highest values are represented by the lightest colors. By the comparative contour it is possible to verify that the lower surface suffers an aerodynamic damage greater than the upper surface since the ice is accreted in that region.

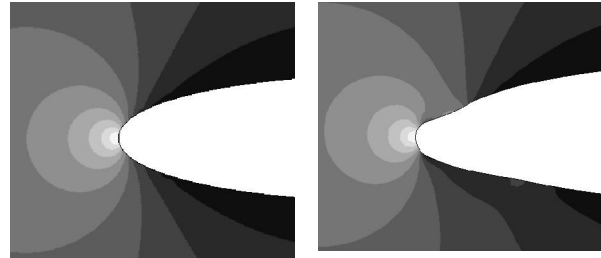


Fig. 17- Pressure contour of the clean airfoil and rime icing for AOA=0°

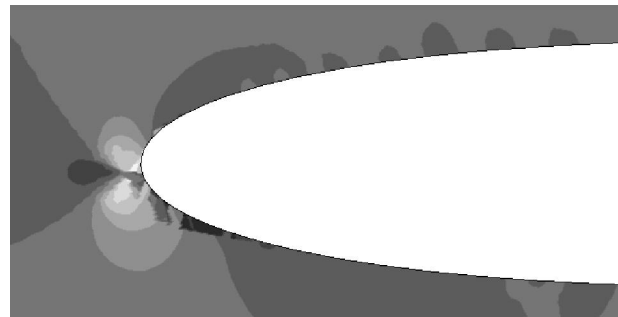
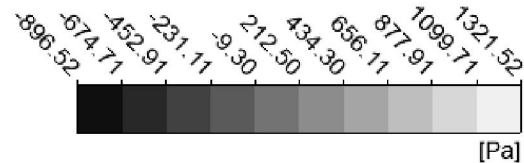


Fig. 18 - Difference between the pressure contours of the clean airfoil and rime icing for AOA=0°

Runs with the clean airfoil were performed at the same Reynolds and Mach in order to compare the coefficients. The C_l maximum decreased about 30% and the minimum C_d increased almost 15%. Fig. 19 and Fig. 20 display the force coefficients.

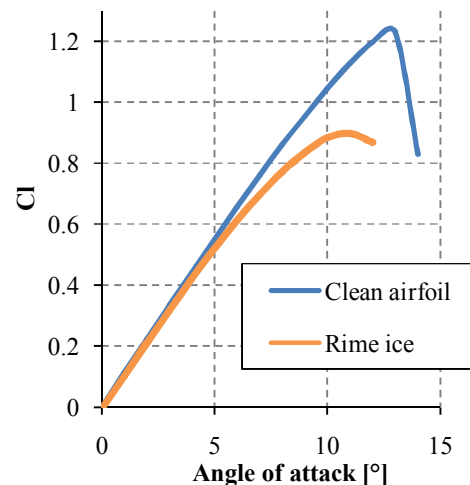


Fig. 19 - C_l versus angle of attack

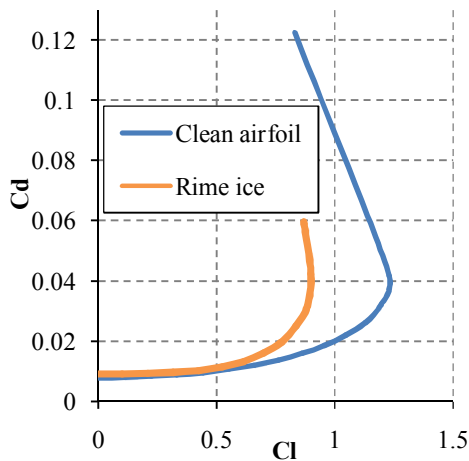


Fig. 20 - C_1 Drag Polar

6 Glaze icing analysis

The next step was performed based on Bragg [3], who simulated this ice accretion in a wind tunnel test. The parameters employed were 2.1 of LWC, 20 μm of MVD and 18 °F (265.4 K) of temperature.

Since all variables considered by FAR 25 [1] are known, it is possible to verify that this accretion does not fit in the envelope specified by the regulation: for these values of LWC and MVD, the temperature should be around -4 °F, as can be seen in Fig. 11 above.

Glaze icing used in numerical simulation with CFX [9] is shown below. This type of shape occurs when the droplets freeze before the region of impact. The final shape is similar to a horn. Fig. 21 show the mesh prepared in ICEM [6]. Flow conditions were $Re = 1.5 \text{ milion}$ and $Mach = 0.12$.

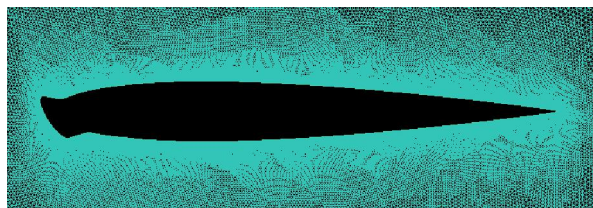


Fig. 21 - Mesh around glaze ice airfoil

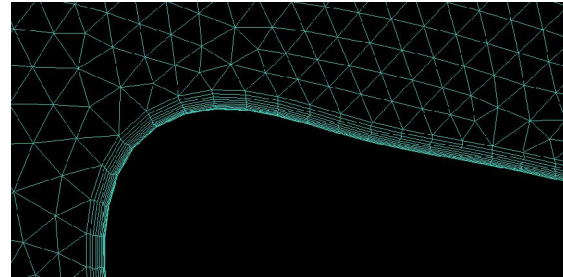


Fig. 22 - Close up view of the mesh around glaze ice airfoil

It is possible to notice, in Fig. 23, the presence of separation bubbles, indicated by the region of constant pressure. The suction peak moves forward. After the bubble, a recovery process is started until the clean airfoil pressure distribution is reached. It can be better observed in Fig. 24: the bubble on the upper surface is more dangerous than that one on the lower. Furthermore, a problem in this CFD analysis can be noticed: the variation of pressure on the curvature changing region of the lower surface is barely detected, and it is represented by the soft disturbance shown in the pressure gradient.

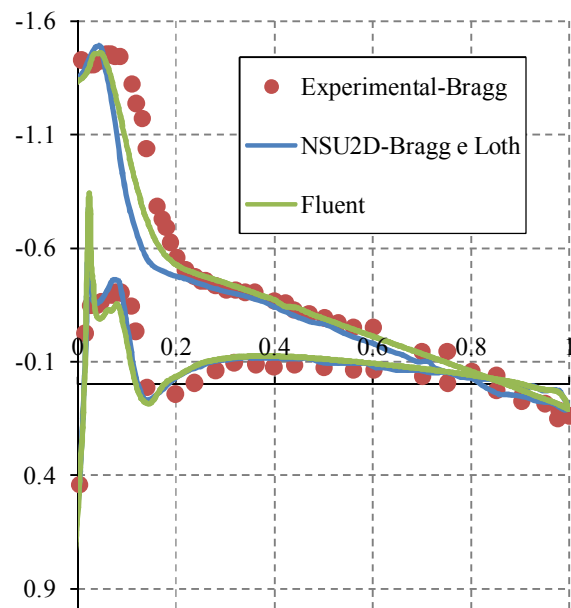


Fig. 23 - Pressure distribution comparison for 4° of angle of attack

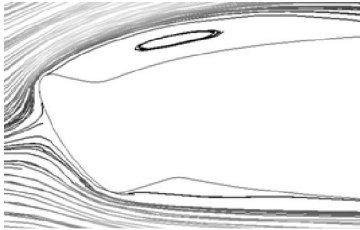


Fig. 24 - Velocity streamlines for 4° of angle of attack

The stall happens because the bubble is not able to reattach to the airfoil as the angle of attack increases, which occurs prematurely at 6°. Another important behavior is that, as the rime iced airfoil, the profile has its symmetrical characteristics compromised, as shown in Fig. 25 (the angle of 0 lift is not 0 anymore). However, it can cause more damage if it occurs to NACA 0012 airfoil, commonly used in horizontal stabilizers. In Fig. 26 it is noticed that the accuracy of lift prediction is not linked to the drag, as the latter is much more dependent on mesh quality.

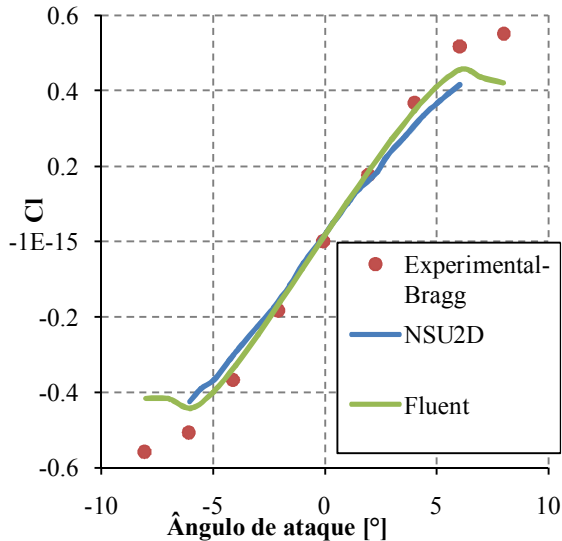


Fig. 25 - C_l versus angle of attack

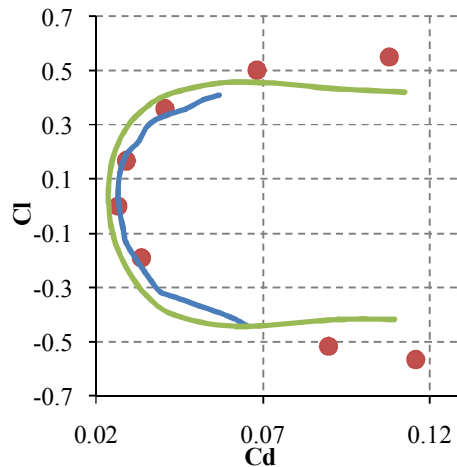


Fig. 26 - Drag Polar

7 Conclusion

It has been presented in this abstract part of a research involving more cases and geometries. The results have shown a good correspondence with the references. However, CFD failed to predict some details since it is quite dependent on the mesh quality and CPU cost. CFD is a powerful tool to evaluate flow behaviors. Nevertheless, some devices to support simulations are needed to provide more confidence in the results obtained and to verify the capability of the model to reproduce the actual flow. Since there is a computational cost involved in the research, the balance between accuracy on the results and CPU time must be considered in order to provide an optimized study.

8 References

[1] Federal Administration. *Federal Aviation Regulations- Part 25, Airworthiness Standards: transport category airplanes, Appendix C*;

[2] Hacker Paul T. and Dorsch Robert G.; “*A Summary of Meteorological Conditions Associated with Aircraft Icing and a Proposed Method of Selecting Design Criteria for Ice-Protection Equipment*”, NACA-TN-2569, November 1951;

[3] Bragg, Michael B.; “*An Experimental Study of the Aerodynamics of NACA 0012 Airfoil with Simulated*

Glaze Ice Accretion”, NASA CR-179897, November 1986;

[4] Bragg, Michael B. e Loth Eric; “*Effects of Large-Droplet Ice Accretion on Airfoil and Wing Aerodynamics and Control*”, DOT/FAA/AR-00/14, March 2000;

[5] Cao, Y. e Zhang Q.; “*Numerical Simulation of Rime Ice Accretions on an Airfoil Using Eulerian Method*”, The Aeronautical Journal, May 2008;

[6] ANSYS, Inc. ANSYS ICEM CFD 12.1 User's Guide, 2009;

[7] ANSYS, Inc. FLUENT, User's Guide, 2009.

[8] Harris, Charles D.; “*Two-dimensional Aerodynamic Characteristics of NACA 0012 Airfoil in the Langley 8-foot Transonic Pressure Tunnel*”, NASA-TM-31927, April 1981;

[9] ANSYS, Inc. ANSYS CFX 12.1 User's Guide, 2009.

9 Copyright Statement

The authors confirm that they, and/or their company or organization, hold copyright on all of the original material included in this paper. The authors also confirm that they have obtained permission, from the copyright holder of any third party material included in this paper, to publish it as part of their paper. The authors confirm that they give permission, or have obtained permission from the copyright holder of this paper, for the publication and distribution of this paper as part of the ICAS2012 proceedings or as individual off-prints from the proceedings.